



In-situ strain measurements in the plastic deformation regime inside casted parts using fibre-optical strain sensors

A contribution to the production of intelligent parts

Florian Heilmeier¹ · Robert Koos² · Klaus Weraneck³ · Markus Lindner⁴ · Martin Jakobi³ · Johannes Roths⁴ · Alexander W. Koch³ · Wolfram Volk¹

Received: 26 July 2018 / Accepted: 7 January 2019 / Published online: 18 January 2019
© German Academic Society for Production Engineering (WGP) 2019

Abstract

Fibre Bragg Gratings (FBGs) were employed as internal strain sensors within tensile specimens that were machined out of a casted aluminium alloy. Embedded FBGs have the potential to directly measure strains within a casted part for a better understanding of load cases for the part design process. In addition, if the FBGs remain in the part, strains can be measured under real-life conditions and return valuable evidence for health monitoring. The proof of application is provided by the presented tests by comparison of external and internal strain measurements. The step-wise calibration test gives evidence for a linear transition between external straining and internal response by the FBGs and thus a constant conversion factor was obtained. The application in a common tensile test proves a precise strain measurement by the FBGs and their durability until a short time before the specimens failed. These findings form the basis for an application of FBGs within real structural parts and thus the production of intelligent parts in future work. As a conclusion, internal strain measurements using FBGs have the potential to provide additional strain data compared to common methods and hence to improve the design process as well as to monitor casted parts under operating conditions.

Keywords Optical sensors · Tensile test · Intelligent part · Casting

1 Introduction

For the design and production of casted structural parts, a profound understanding of the interaction of material properties, the geometrical shape and the operational loads is needed. Simulations under load conditions give indication for the occurrence of strains within a part. These simulations

need to be validated using precise strain measurements within real parts.

In-situ measurements give evidence for process-induced strains while casting and thus the resulting internal loads within a casted part. State of the art methods incorporate non-destructive measurements like diffraction methods which can utilize X-rays from lab sources, as well as neutron and synchrotron radiation. For example, Wagner et al. investigated intergranular straining during tensile tests with Inconel 718-specimens using neutron diffraction [1]. Reihle et al. used neutron diffraction to measure insitu strains during casting aluminium around steel inserts [2] and Drezet et al. for the determination of the rigidity point when castings are firstly able to transfer stresses while solidification [3].

Ex-situ measurements are applicable for the investigation of strain reactions induced by internal and external loads. Strain gauges are used for mechanical investigations such as the hole drilling method, which has been suggested by

✉ Florian Heilmeier
fhe@utg.de

¹ Institute of Metal Forming and Casting, Technical University of Munich, Garching, Germany

² Research Neutron Source Heinz Maier-Leibnitz, Technical University of Munich, Garching, Germany

³ Institute for Measurement Systems and Sensor Technology, Technical University of Munich, Munich, Germany

⁴ Photonics Laboratory, Munich University of Applied Sciences, Munich, Germany

Mathar for the first time [4]. It is used for the examination of internal stresses by cutting out material and thus disturbing the internal force equilibrium. This leads to strains, which are being measured by strain gauges and form the basis of stress calculations.

Strain gauges can also be used within a wide range of measurements under real-life load conditions [5]. Due to that, validation measurements are most commonly carried out by using strain gauges. One major disadvantage, however, is the fact that they are only applicable for near-surface measurements of strains. Strains within the part can thus only be obtained by calculations.

Although the presented in-situ methods may provide depth-resolved strain data, they are only applicable for small parts in a laboratory environment and are impossible to be used under real-life conditions. An alternative is given by embedded FBGs. Recent efforts on structural health monitoring incorporate fibre-optical strain sensors, so-called Fibre Bragg Gratings (FBGs). Strain gauges may be replaced by FBGs for near-surface strain measurements [6], or integrated into composite parts such as glass fibre or carbon fibre composites at present [7, 8].

Based on this principle, and due to the fact that common methods only cover near-surface strains and depth-resolved methods are hardly available for industrial purposes, FBGs are proposed as internal strain sensors for monitoring casted parts under external loads. Weraneck et al. showed that glass fibres with Bragg gratings can withstand casting into aluminium alloys and that they are able to measure strains in-situ and time-resolved during solidification and cooling [9]. Lindner et al. used an array of capsuled regenerated FBGs to monitor the temperature distribution during an aluminium cast process [10]. As the FBGs remain inside the part after casting, they may be used as internal strain sensors subsequently. The strain information from within a casted part is of particular significance as strains inside the part cannot be measured in-situ under real-life conditions. In order to show the feasibility of internal strain measurements using FBGs, instrumented tensile specimens are tested and evaluated for further monitoring of structural parts.

2 Materials and methods

2.1 Casting

In order to obtain tensile specimens containing working FBGs, a casting geometry for tensile specimen green bodies was used. It consists of an inlet with a filter and two runners which direct the alloy into two identical specimens and their feeders, as shown in Fig. 1a. The green bodies (Fig. 1b) are cone-shaped to support a directional solidification from bottom to top.

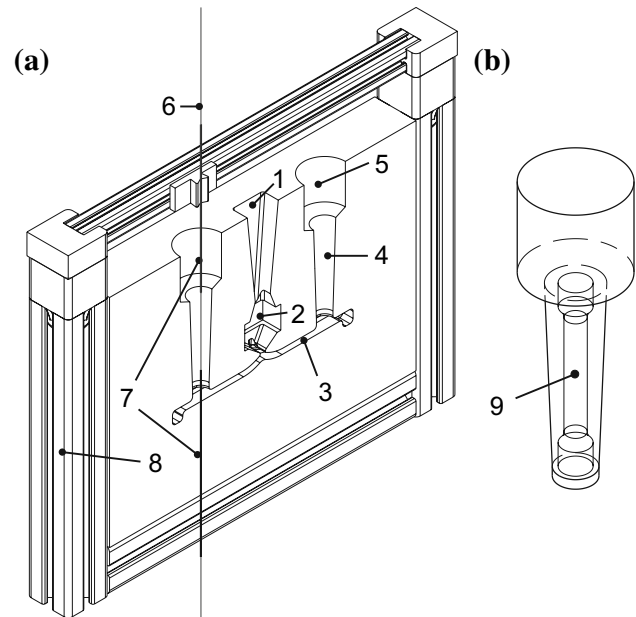


Fig. 1 **a** Sketch of one half of the casting mould for casting tensile specimen green bodies containing FBGs. The alloy is poured into the inlet (1) and reaches the filter (2). The runners (3) lead the melt into two identical specimens (4) which have a feeder on top (5). The fibre (6) is located in the axis of the specimen and is guided by two steel capillary tubes (7) which are mounted on a frame (8). **b** Sketch of the specimen (9) with a diameter of 8 mm and a test length of 40 mm within the green body. It is machined conforming to [11]

The handmade mould consists of oil sand, an oil bonded moulding sand with 91% silica sand, up to 7% process oil and up to 2% other additives. The sand is framed by aluminium profiles which provide both stability and mounting points for the steel capillary tubes which guide the glass fibre and protect it from mechanic forces. The casting process itself is as described by Weraneck et al. [9].

2.2 Material

The cast alloy used for the experiment is the hypoeutectic AlSi9Cu3(Fe) [12], a standard engineering alloy, also known as Al226 and alloy 380. It is a material for structural parts which is used, for instance, for high pressure die casting as well as die casting and sand moulds. Due to its persistence against hot tearing it is suitable for casting complex geometries like cylinder heads and crankcases [13]. Both the standardized composition and the measurement of the alloy's composition are shown in Table 1 in per cent by weight. The composition has been obtained by spark emission spectroscopy using raw material out of a bloom.

A representative micrograph of the alloy from a specimen which has been obtained by a reference casting is shown in Fig. 2. It displays the characteristic phases of Al226 and the embedded fibre bonded with the surrounding microstructure

Table 1 Standardised composition compared to the measured composition of AlSi9Cu3(Fe) (Al226)

Type [wt%]	Al226 (standard)	Al226 (measured)
Si	8.0–11.0	8.5
Fe (max.)	1.3	0.71
Cu	2.0–4.0	2.3
Mn (max.)	0.55	0.24
Mg	0.05–0.55	0.21

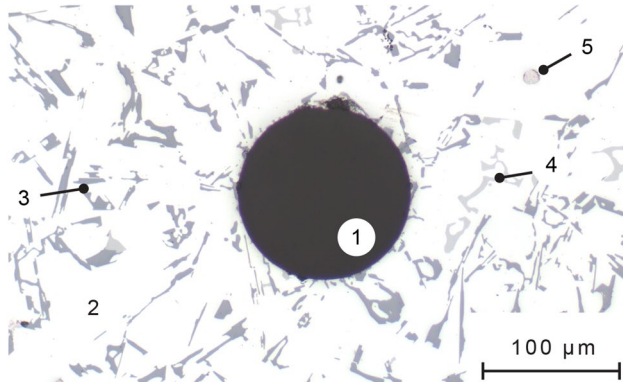


Fig. 2 Micrograph of an embedded fibre (1) within the aluminium alloy at a magnification of 100x. The alloy consists of the primary α -aluminium (2), the eutectic (3) and aluminides (4, 5). The fibre is connected to the alloy force-locked

of the alloy. Light optical microscopy (LOM) captures have been obtained with a Zeiss Axioplan 2 microscope utilizing a Zeiss AxioCam MR5 camera. For the purpose of porosity evaluation an average of 85 micrographs were used to combine into a large area overview of the specimen presented in Fig. 5 as an example.

2.3 Test procedure

Specimens: The casting process allows the manufacturing of green bodies containing FBGs. The tensile specimens are machined out of the green bodies, as can be seen in Fig. 1b, and the FBGs are used for internal strain measurements subsequently. The specimens with a diameter of 8 mm and a test length of 40 mm are conforming to [11].

Tensile testing machine: The experiments have been carried out using a tensile testing machine Zwick 1484 DUPS-M which provides a maximum force of 200 kN. The setup in Fig. 3 incorporates both extensometer strain measurement on the surface and FBG strain measurement inside the specimen.

Interrogator and fibres: For the FBG measurements we used a National Instruments interrogator PXIe-4844 and a

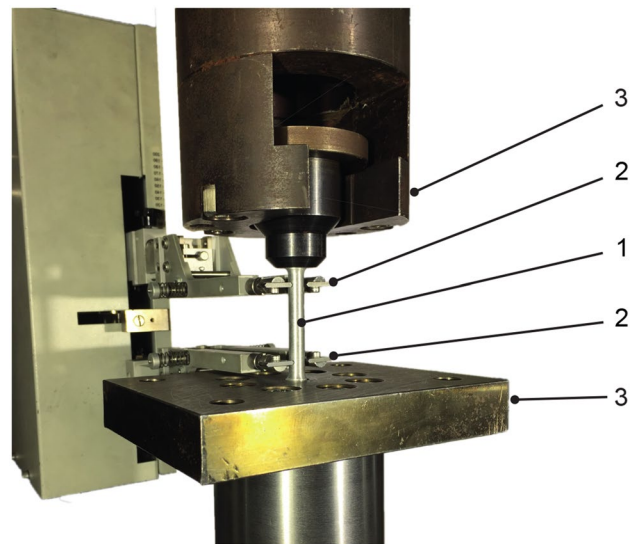


Fig. 3 Experimental setup with the specimen (1), extensometer (2) and mounting system (3). The FBG has been casted into the alloy and is located in the rotation axis of the specimen

PXIe-1073 controller. The interrogator provides a resolution of 0.004 nm within a range of 80 nm. The femtosecond FBGs we used are inscribed into a SMF28-fibre by a infrared femtosecond-pulsed laser. The initial wavelength λ_B is 1550 nm at a grating length of 3 mm.

Test routines: Two test routines were chosen for the characterization of internal strain measurements. A standard tensile test according to [14] is used to evaluate the strain transition between FBG and surrounding aluminium. The tensile test has been carried out strain controlled with a constant strain rate of $2.5 \times 10^{-4} \text{ s}^{-1}$. In the second test routine, a specimen was loaded force controlled with increasing steps of 175 N and a holding time of 240 s, subsequently followed by a release of the force for another 240 s. Each increase and decrease was carried out at a strain rate of $2.5 \times 10^{-4} \text{ s}^{-1}$.

Every specimen was pre-loaded with a force of 50 N which was zeroed before subsequently following the tensile test, that was carried out until sample failure.

3 Analysis

3.1 Fibre Bragg gratings

The basic structure of an FBG is depicted in Fig. 4a. The measurement principle was described by [15] and others, where the resonance wavelength of the reflection is called Bragg wavelength λ_B and is determined by the effective refractive index n_{eff} and the grating period Λ . The mathematical relationship can be seen in Eq. 1 in its primal form [16]:

$$\lambda_B = 2 \cdot n_{eff} \cdot \Lambda. \tag{1}$$

The value of λ_B can be affected by multiple parameters. Eq. 2 shows the dependency of the Bragg wavelength shift $\Delta\lambda_B$ on the strain ϵ_z , the photoelastic coefficient p_e , the initial Bragg wavelength λ_0 , the thermo-optic constant γ and the thermal expansion coefficient α [17, 18]:

$$\Delta\lambda_B = \lambda_0 \cdot [(1 - p_e) \cdot \epsilon_z + (\alpha + \gamma) \cdot \Delta T], \tag{2}$$

p_e is normally within the range of 0.205–0.230 [18, 19]. Temperature variations induce a shift of the Bragg wavelength due to the impact of α with a value of around $0.55 \times 10^{-6} K^{-1}$ for Ge-doped silica glass. γ can be specified as $\gamma = 8.6 \times 10^{-6} K^{-1}$. [18, 20]

Additionally, another aspect has to be taken into account when FBGs are embedded in a solid body. Due to transversal contraction in the specimen, two additional strains ϵ_x and ϵ_y can appear besides ϵ_z . The indices in this nomination refer to Fig. 4a. Here, two local refractive indexes are created [22] and the reflection will consist of two more separated peaks if the difference between ϵ_x , ϵ_y and ϵ_z is significant. In case of knowing the values of ϵ_x and ϵ_y , the peak shifts due to transversal contraction can be calculated with Eq. 3

$$\frac{\Delta\lambda_{B,y} - \Delta\lambda_{B,x}}{\lambda_B} = \frac{n_0^2}{2} (p_{12} - p_{11}) (\epsilon_y - \epsilon_x), \tag{3}$$

according to [23, 24].

The resonance wavelength of the FBG is primarily affected in ϵ_z -direction by the external straining of the tensile test. In case of a distinct peak wavelength caused by ϵ_z , Eq. 3 can be neglected. As a result, for measurements with embedded FBGs in tensile specimens in an air-conditioned environment, Eq. 2 reduces to

$$\frac{\Delta\lambda}{\lambda} = k \cdot \epsilon_z, \tag{4}$$

where $\frac{\Delta\lambda}{\lambda}$ is measured and k may be derived when ϵ_z is known.

3.2 Peak detection

For this work we developed a peakfinding algorithm based on MATLAB-functions [25], which allows the detection of all distinct peaks over time and external straining ϵ_z subsequently with respect to Eq. 3. Each time frame of a spectrum is filtered by using a Kaiser window above a noise level of -39.4 dBm. The peaks, which are found afterwards by the function, are labeled independently. The width $\Delta\lambda$, in which one peak may shift from one time frame to the other, depends on the constant external strain rate and is fixed at ± 0.2 nm. The algorithm is visualized in form of a Nassi-Shneiderman-diagram in Fig. 4b. All relevant functions, parameters and values are given in Table 2.

3.3 Porosity evaluation

The porosity is derived from LOM micrographs of tested specimens. Therefore image segmentation [26] was utilized to distinguish voids from the surrounding microstructure of the alloy as detailed in Fig. 5. The area of the highlighted voids in pink colour, related to the total selected area in green colour, is used to calculate the porosity ϕ :

$$\phi = \frac{\sum \text{pore areas}}{\text{total selected area}}. \tag{5}$$

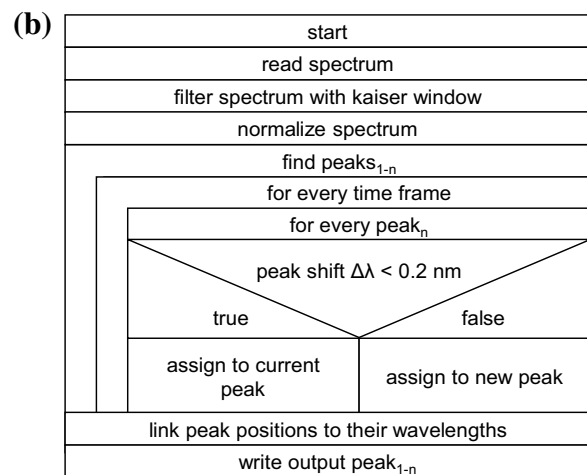
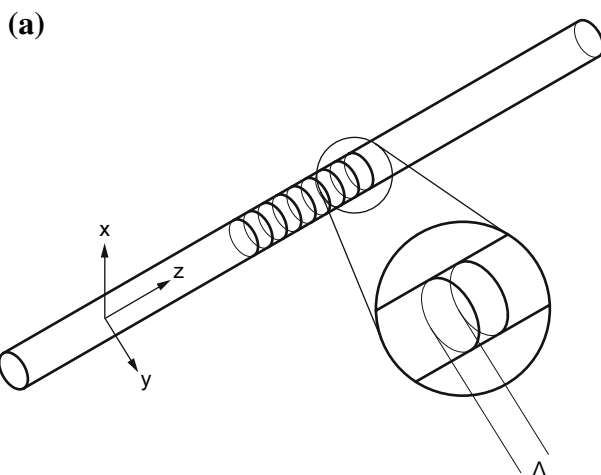


Fig. 4 **a** Basic structure of a FBG with the coordinate system as used by the authors. A standard fibre is used to inscribe periodic modulations of the refractive index. A broadband IR-spectrum is employed

as input. One part of the light is transmitted and the other part is reflected according to Eq. 1. **b** Nassi-Shneiderman-diagram of the peakfinding-algorithm

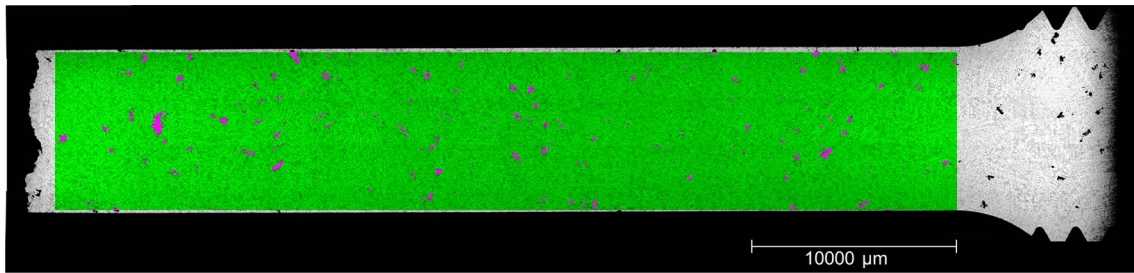


Fig. 5 Combined LOM-micrograph of ZS18 at a magnification of $\times 25$ after tensile testing. Note the fracture surface on the left side. The voids are highlighted in pink colour and the porosity is derived from the fraction of the voids within the total binarized selected area in green colour

The greyscale thresholds used for segmentation are chosen from a best fitting selection. An estimation of the errors is achieved by variation of these thresholds by a constant higher and lower value.

4 Results

4.1 Step-wise calibration test

This test routine was designed to evaluate the applicability of FBGs as internal strain sensors in casted parts under external load and for calibration purposes. Therefore, one specimen was charged 51 times with a rising load (in-situ steps) until the specimen failed (see Fig. 6). The sections where the specimen was released (ex-situ steps) give evidence for plastification of primary α -aluminium because strains do not reach the neutral line again.

For both the in-situ and ex-situ steps the external straining and the internal response of the FBG can be compared. Figure 7a shows the data couples of the in-situ and ex-situ steps with a linear fit which begins in the origin of the chart. Note the slight deviation between the linear fit and the ex-situ data couples. In order to calculate strains from the FBG data, Eq. 4 is converted to

$$k = \frac{\Delta\lambda}{\lambda \cdot \epsilon_z}, \tag{6}$$

and thus the corresponding k-factor can be depicted from the linear fit in Fig. 7a. It represents the measured data for both ϵ_z and $\frac{\Delta\lambda}{\lambda}$. k can be depicted as $k = 0.7418$ according to Eq. 6 by determination of the slope. For an estimation of the expected error made by the linear fit, Fig. 7b shows the deviation of the compared strains from the fitted line in Fig. 7a. The maximum deviation lies in between a strain of 1.0×10^{-4} and thus the measurement uncertainty is within 3.2%. For the subsequent strain measurements within casted

Table 2 Parameters for the peakfinding-algorithm using MATLAB-functions

function	Parameter	Value
'findpeaks'	MinPeakProminence	0.05
'findpeaks'	MinPeakHeight (normalized)	0.98
'kaiser'	L, beta	25, 1
–	$\Delta\lambda$	0.20 nm
–	noise limit	–39.4 dBm

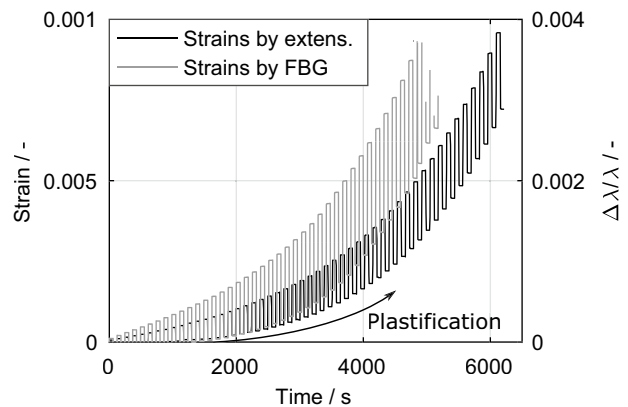


Fig. 6 Strains by extensometer and by FBG versus time. The arrow marks the area where plasticity occurs as the ex-situ steps do not reach the abscissa any more

aluminium parts the resulting k-factor = 0.7418 will be used with respect to the uncertainty of 3.2%.

4.2 Standard tensile test

The application of FBGs as internal strain sensors took place in a standard tensile test. The corresponding external strain curves for all tested specimens are shown in Fig. 8a. The strain evolution below the yield strength (0.2 %) does not follow a linear path and thus only the subsequent sections are used for the linear approximations. The time-related

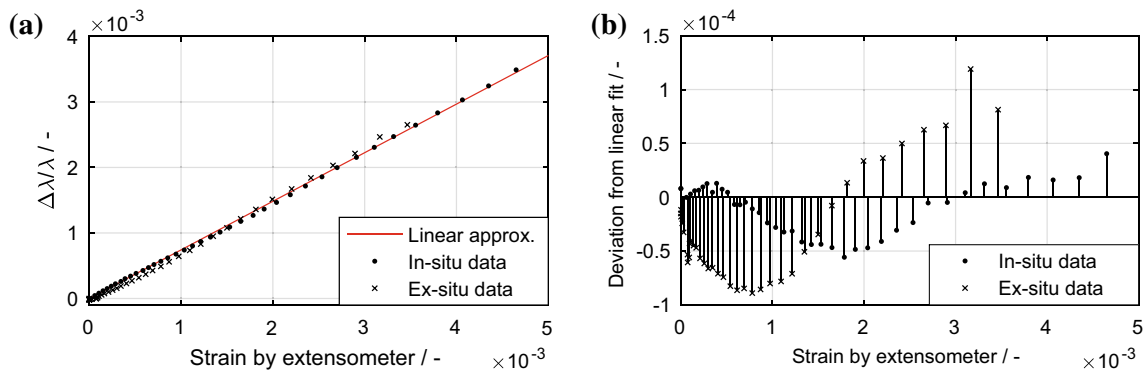


Fig. 7 a Pair-wise comparison of the data couples obtained from specimen FS18. The linear approximation shows that the response behaviour is nearly linear yet not perfectly precise for the ex-situ val-

ues. **b** Deviations of the compared values in Fig. 7a from the linear fit versus external straining which result in a maximum uncertainty of 3.2% for subsequent strain measurements

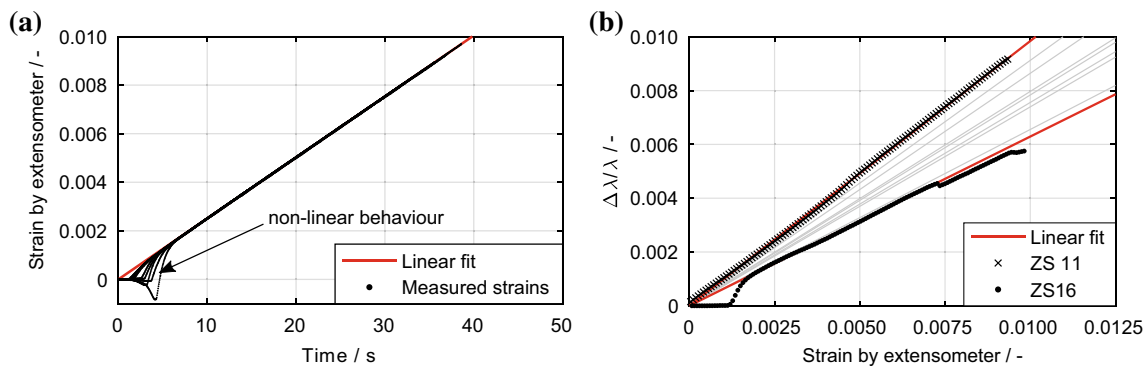


Fig. 8 a Strain curves of all tensile tests with a strain rate of $2.51 \times 10^{-4} s^{-1}$. The non-linear start behaviour has been excluded from the linear approximation which starts in the origin of the chart. **b** $\frac{\Delta\lambda}{\lambda}$ versus external strain for all specimens. The data couples are

shown exemplarily for the specimens ZS11 and ZS16 and their linear fits are highlighted in red colour. The intersection of the fits with the abscissa define the origins of all measured data

starting point is defined as the intersection of the fits with the abscissa and is shifted to the origin.

Assuming an ideal strain transition between aluminium and fibre, the measured strains by the FBGs have to be linear with an uniform slope. Figure 8b shows the strains by FBG measurement versus external straining for the specimens ZS11 and ZS16. Again, the start behaviour is not necessarily linear, followed by a linear increase of strain which is used to fit a linear regression. The point of origin is defined as intersection of the corresponding line and the abscissa. The slopes of ZS11 and ZS16 form the highest deviation of all measurements and are chosen for further comparison. In addition, the linear fits of the remaining tensile tests are plotted in grey colour to show the variance of the strain responses measured by FBGs.

In order to calculate strains from the FBG data, Eq. 6 is used to derive the corresponding k-factor. The linear fits in Fig. 8b represent the measured data for ϵ_z and $\frac{\Delta\lambda}{\lambda}$, respectively. k is depicted by determination of the slopes for each

measurement. The results are shown in Table 3 for a constant external strain rate of $2.51 \times 10^{-4} s^{-1}$.

The variance of the k-values shows that for applications in real parts each FBG should be calibrated separately. If the calibration value for k is applied to an FBG measurement and the errors are derived from the min and max-values in table 3, the uncertainty will rise with the value of $\frac{\Delta\lambda}{\lambda}$ according to Fig. 9a and lead to a maximum error of 24%. Instead, if the FBG-strains are each calculated with their own k-values, the strains are far more accurate (see Fig. 9b).

4.3 Evaluation of the FBG-spectra

In order to assess the quality of measurements with FBGs in aluminium, the spectra of the FBGs need a detailed analysis. Weranek et. al. states that multiple micro strains within the aluminium in the measuring zone of the FBGs can lead to double refraction [9], and thus two or more peaks can be observed. The FBG-spectra obtained during external

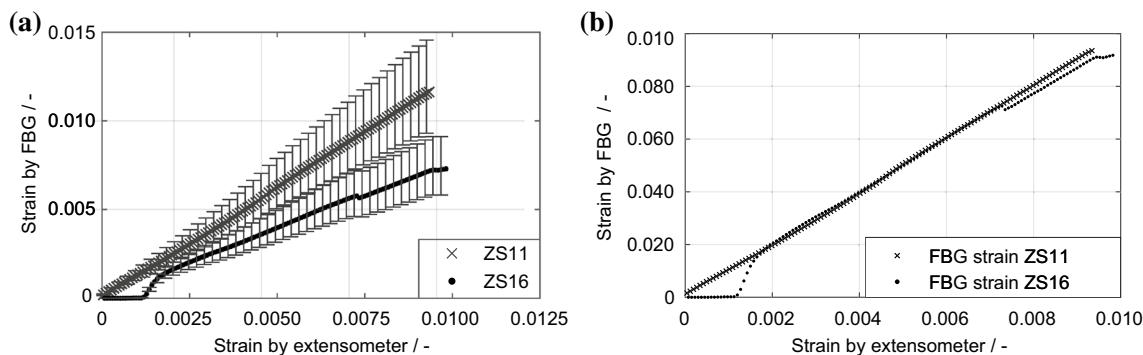


Fig. 9 **a** Calculated strains for ZS 11 and ZS 16 out of $\frac{\Delta\lambda}{\lambda}$ using the calibration, min and max values of k. For a better visibility only every third errorbar has been plotted. **b** Calculated strains for ZS11 and ZS16 out of $\frac{\Delta\lambda}{\lambda}$ using the exact value of k each

straining give evidence for the occurring superpositions of single peaks which may be caused by ϵ_x and ϵ_y as specified in Eq. 3. Thus, the excess peaks have to be separated from the one peak caused by ϵ_z , which will be used for the investigation of internal strains. Hence, Fig. 10a, b show the spectra for the specimen ZS11 and ZS16 exemplarily before the test, with half the maximum strain and a short time before failure. The arrows mark the local positions of the primary peak, which represents ϵ_z and is defined as the highest peak before the test. The normalized intensity of the spectra on the ordinate decreases over time while the peak is pulled to higher wavelengths. Also, secondary peaks rise in intensity and might even overtop the primary peak shortly before failure. The peak positions are derived from the spectra according to the algorithm shown in Fig. 4b for each time frame and are shown for ZS11 and ZS 16 in Fig. 11a, b, respectively. Each significant local intensity maximum is marked with an unique label in order to track the peaks over time. We are thus able to clearly distinguish between the

primary and secondary peaks as long as the peak positions are distinguishable. Figure 11a, b exemplarily show that the progression of the primary peak is linear for both measurements. Note that the primary peak of specimen ZS16 gets overlain by another peak, as can be seen in spectrum 2 in Fig. 10b. The peak finding algorithm is thus not able to distinguish between two peaks, and this is why $\frac{\Delta\lambda}{\lambda}$ shifts to smaller values in Fig. 11b.

4.4 Evaluation of the porosity

The sand mould-casted aluminium exhibits porosity which can mitigate the transmission of external strains to the fibre by exceeding promotion of strains through voids [27]. Therefore, the k-values of eight specimens are shown as a function of the post mortem porosity in Fig. 12. The specimens form two groups, which are highlighted in this view and result from two batches casted on two different days weeks apart from each other. There is a gap between the post mortem

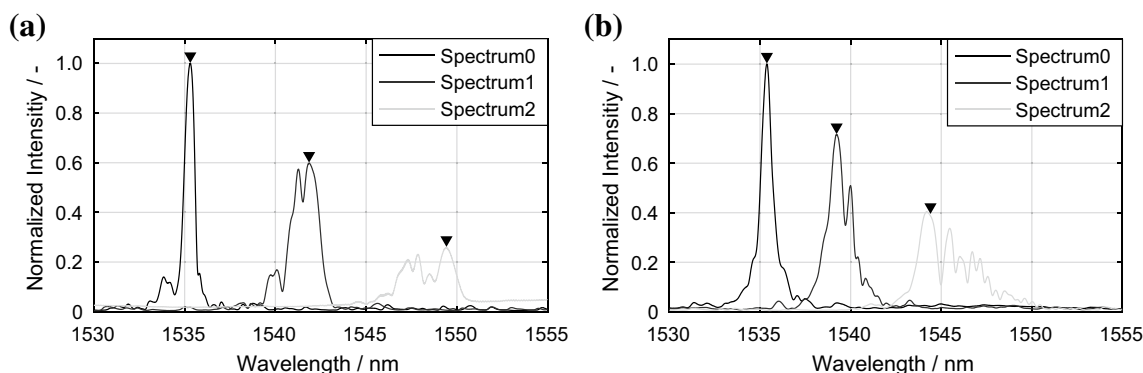


Fig. 10 **a** Spectra of specimen ZS11 versus time without any load (0), with half the maximum load (1), and just before failure (2). The spectrum degenerates and broadens under the influence of external straining. The intensities of the reflected peaks decrease continuously while birefringence occurs at high strains. **b** Spectra of specimen ZS16 ver-

sus time without any load (0), with half the maximum load (1), and a short time before failure (2). The spectrum degenerates just like in (a). In addition, the primary peak gets overlain by another peak with nearly the same wavelength

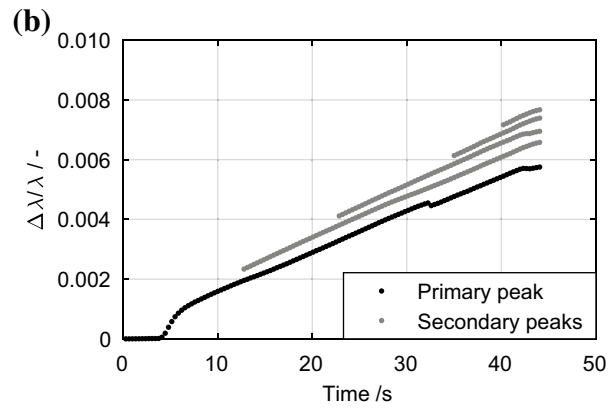
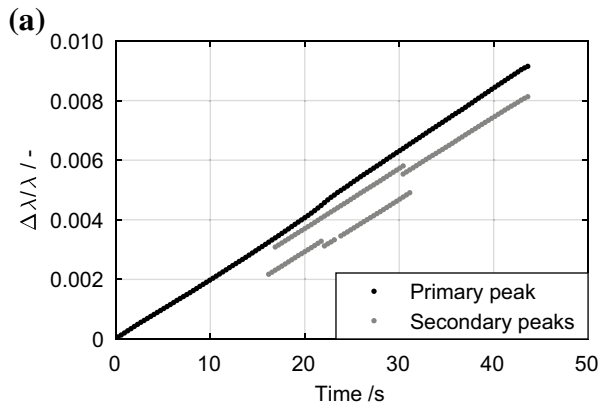


Fig. 11 **a** Positions of the primary and secondary peaks of specimen ZS11 versus time. The primary peak shows a linear progression over time. This gives evidence that birefringence does not affect the strain response of the primary peak which represents ϵ_z . **b** Positions of the

primary and secondary peaks of specimen ZS16. The primary peak again shows a linear progression over time but gets overlain by a secondary peak and thus the peak position shifts to lower wavelengths

Table 3 k-factors for the specimens containing FBGs

Test spec.	k-factor/-	Test spec.	k-factor/-
ZS 08	0.7366	ZS 17	0.6530
ZS 11	0.9805	ZS 18	0.7806
ZS 12	0.9088	mean	0.7882
ZS 13	0.7938	min	0.6267
ZS 14	0.7530	max	0.9805
ZS 15	0.8610	FS18	0.7418 (calibration)
ZS 16	0.6267		

k is derived based on the measurements of both $\frac{\Delta\lambda}{\lambda}$ and ϵ_z with a resulting uncertainty of $\pm 1.0 \times 10^{-4}$ each

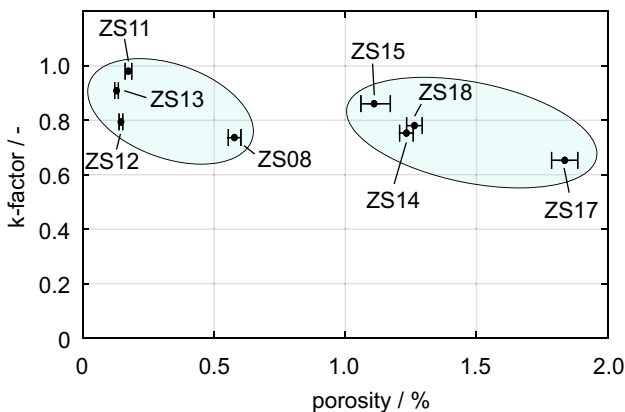


Fig. 12 k-factors of eight tensile specimens versus their post mortem porosity. Two groups with a slight dependency of the k-factors on the porosity are highlighted and can be related to the casting conditions on two different days of production

porosities below 0.6 % and above 1.1 % which can be related to different casting conditions. A slight dependency of the k-factors on the groups is recognizable even though the differences are marginal compared to the overall deviation of all k-factor values.

5 Discussion

The step-wise tensile test shows the effect of strain transition between aluminium and fibre. The evaluation is divided into in-situ (steps under load) and ex-situ (steps free of load) measurements. This enables the direct comparability of strains measured by extensometer and FBG without the need for fitted models. The evolution of plastic behaviour can be derived from the propagation of the ex-situ values. Each data couple in Fig. 7a represents one strain value which is held for 240 seconds. The ex-situ data couples shown in Fig. 7a indicate the occurrence of plasticity within the specimen. The fact that both the in-situ and ex-situ values show nearly exact linear behaviour enables the generation of distinct transfer functions and thus precise internal strain measurements with an uncertainty of 3.4 % due to plastification within the aluminium. The correlation of strains measured by extensometer and FBG by using a linear calibration function will enable the generation of, for example, intelligent casting parts subsequently.

The tensile tests presented in Fig. 8a were strain controlled and a constant strain rate could be shown. The strain response of the extensometer displays non-linear behaviour for strains up to yield strength (0.2%) caused by the settling of the mechanic setup despite preloading with

a force of 50 N. Hence only the measured points above 0.2 % strain are used for the linear approximations. The resulting slope of $2.51 \times 10^{-4} s^{-1}$ shows that the desired strain rates of all tensile tests were reached as intended. The subsequently derived response of the internal strain measurement is linear yet not of a constant slope over all measurements. The variation in FBG responses is presented in Fig. 8b. The linearity of each response indicates that the FBGs are connected to the aluminium enabling effective load transfer.

The reason for non-uniform responses of the FBGs may be induced by the casting process itself. The k-factors as a function of porosity shown in Fig. 12 indicate a slight dependency caused by the as-cast condition of the aluminium generating two groups below and above porosity levels of 1 %. These groups represent two batches of different casting conditions influencing the microstructure of the Al alloy and thus the investigated post mortem porosity.

The fibres have been positioned in the moulds by hand and may be contributing to an undefined impact on the strain transmission causing slight deviations between external straining and measured internal strains.

Impurities and voids, especially located on the surface of the fibre, can also affect the strain transition. As a disturbing factor during form filling, the fibre gets bathed by aluminium during casting and thus the attachment of debris and gas pores is probable.

In practice, if every cast-in FBG is calibrated separately, no effect on the precise measurement of internal strains can be expected, as demonstrated in Fig. 9b. Here, a consideration of the 3.4 % uncertainty derived from the step-wise test is recommended with respect to the fact, that real loads are commonly pulsating and not linear increasing like in standard tensile tests.

The spectra show not only the primary peak, which is used to determine the internal strains, but also secondary peaks. The peak shapes transform with the increasing external strains, similar to the calculations by Müller et al. [28]. It is possible that additional peaks appear as others vanish. This necessitates the detection of more than one peak during the strain measurement, which is only reasonable if the primary peak is still of significance. The appearance of secondary peaks may be traced to microstrains within the aluminium, which are induced by discrete grains or porosity at microscopic scales. Another reason for the occurrence of secondary peaks may be the influence of straining on the fibre orthogonal to its z-axis, as considered in Eq. 3.

However, the presented tests show that the external straining ϵ_z can be traced down to the primary peak and thus the influence of birefringence caused by micro strains or by transversal strains can be excluded from technical strain measurements.

6 Conclusion and outlook

The performed tests show the applicability of FBGs as internal sensors in casted parts for precise in-situ strain measurements. Ten tensile specimens have been investigated within two test routines incorporating calibration and standard tensile tests.

The analyzed data shows that cast-in FBGs are capable of measuring internal strains under external loads. When calibrated separately, each FBG delivers precise strain data from within the part. The occurrence of secondary peaks in the FBG-spectra gives evidence of microstrains or transversal straining from surrounding bulk material. This interesting topic will be the subject of further investigations in the field of microstructural analysis. Another continuative consideration incorporates transmission techniques like computed microtomography, which allows an evaluation of the interface of the fibre as well as the surrounding microstructure.

Compared to common strain measurements, the new approach of measuring internal strains enables a better understanding of load-related reactions within a casted part. This establishes a new possibility for the design process to be extended by in-situ data of strains.

For further research in the field of intelligent parts, the FBGs may remain in the casting which can be tested under operating conditions. The obtained data will give valuable input for health monitoring applications.

Acknowledgements The authors like to thank the Deutsche Forschungsgemeinschaft (DFG) for funding this project under grant No. VO 1487/11-1, KO 2111/11-1 and RO 4145/3-1.

References

1. Wagner JN, Hofmann M, Wimpory R, Kremaszky C, Stockinger M (2014) Microstructure and temperature dependence of intergranular strains on diffractometric macroscopic residual stress analysis. *Mater Sci Eng A* 618:271–279
2. Reihle M, Hofmann M, Wasmuth U, Volk W, Hoffmann H, Pety W (2014) In-situ strain measurements during casting using neutron diffraction. *Mater Sci Forum* 768–769:484–491
3. Drezet J, Mireux B, Szaraz Z, Pirling T (2017) In situ neutron diffraction during casting: determination of rigidity point in grain refined al-cu alloys. *Materials* 7:1165–1172
4. Mathar J (1933) Ermittlung von Eigenspannungen durch Messung von Bohrloch-Verformungen. *Archiv für das Eisenhüttenwesen* 6(7):277–281
5. Window AL (1992) *Strain gauge technology*. Elsevier Applied Science, London
6. Li WY, Cheng CC, Lo YL (2009) Investigation of strain transmission of surface-bonded FBGs used as strain sensors. *Sens Actuators A* 190:201–207
7. Manner S (2016) *Validation of a hybrid Sensor Network for Helicopter Rotor Blades*, Dissertation. Technische Universität, München

8. de Oliveira R, Ramos CA, Marques AT (2008) Health monitoring of composite structures by embedded FBG and interferometric Fabry–Pérot sensors. *Comput Struct* 86:340–346
9. Weraneck K, Heilmeier F, Lindner M, Graf M, Jakobi M, Volk W, Roths J, Koch AW (2016) Strain measurement in aluminium alloy during the solidification process using embedded fibre bragg gratings. *Sensors* 16:1853–1870
10. Lindner M, Tunc E, Weraneck K, Heilmeier F, Volk W, Jakobi M, Koch AW, Roths J (2018) Regenerated Bragg grating sensor array for temperature measurements during an aluminium casting process. *IEEE Sens* 18(13):5352–5360
11. DIN 50125:2016-12 (2016) Prüfung metallischer Werkstoffe - Zugproben. Deutsches Institut für Normung e.V
12. ISO 3522:2007 (2007) Aluminium and aluminium alloys—Castings—Chemical composition and mechanical properties. International Organization for Standardization
13. BDG (2017) Bundesverband der Deutschen Gießereindustrie: Sand- und Kokillenguss aus Aluminium. Bundesverband der Deutschen Gießerei-Industrie, Düsseldorf
14. ISO 6892-1:2016 (2016) Metallic materials—tensile testing—part 1: method of test at room temperature. International Organization for Standardization
15. Kashyap R (1997) *Fiber Bragg gratings*, 2nd edn. Academic Press, London
16. Erdogan T (1997) Fiber grating spectra. *J Lightwave Technol* 15(8):1277–1294
17. Rao Y (1997) In-fibre Bragg grating sensors. *Meas Sci Technol* 8:355–375
18. Othonos A (1997) Fiber Bragg Gratings. *Rev Sci Instrum* 68:4309–4341
19. Jülich F, Aulbach L, Wilfert A, Kratzer P, Kuttler R, Roths J (2013) Gauge factors of fibre Bragg grating strain sensors in different types of optical fibres. *Meas Sci Technol* 24:094007 (7pp)
20. Morey WW, Meltz G, Glenn WH (1990) Fiber optic Bragg grating sensors. *Proc SPIE* 1169:98–107
21. Werneck MM, Allil RCSB, Ribeiro BA, de Nazaré FVB (2013) A guide to fiber bragg grating sensors. In: Cuadrado-Laborde C (ed) *Current trends in short- and long-period fiber gratings*. IntechOpen. <https://doi.org/10.5772/54682>. Available from: <https://www.intechopen.com/books/current-trends-in-short-and-long-period-fiber-gratings/a-guide-to-fiber-bragg-grating-sensors>
22. Othonos A (1999) *Fibre Bragg grating: fundamentals and applications in telecommunications and sensing*. Artech House, London, pp 352–356
23. Gafsi R, El-Sherif MA (2000) Analysis of induced-birefringence effects on fiber Bragg gratings. *Opt Fiber Technol* 6:299–323
24. Urban F, Kadlec J, Vlach R, Kuchta R (2010) Design of a sensor based on optical fiber bragg grating lateral deformation. *Sensors (Basel, Switzerland)* 10:11212–11225
25. MATLAB (2018) *Signal Processing Toolbox User's Guide Release 2016b*, The MathWorks, Inc., Natick, Massachusetts, United States
26. MATLAB (2018) *Image Processing Toolbox User's Guide, Release 2016b*. The MathWorks Inc, Natick, Massachusetts, United States
27. Shen Y-L (1997) Combined effects of microvoids and phase contiguity on the thermal expansion of metal-ceramic composites. *Mater Sci Eng A* 237:102–108
28. Müller MS, Buck TC, El-Khozondar HJ, Koch AW (2009) Shear strain influence on fiber Bragg grating measurement systems. *J Lightwave Technol* 27(23):5223–5229